Article

Geminal $^{13}C-^1H$ NMR Spin-Coupling Constants in Furanose Rings: New Empirical Correlations with Conformation

Reagan J. Meredith, Ian Carmichael, and Anthony S. Serianni*

Read Online

ACCESS | Metrics & More | Article Recommendations | Supporting Information

ABSTRACT: Density functional theory (DFT) calculations have been used to develop a new approach to interpreting geminal (two-bond) $^2J_{CCH}$ NMR spin-coupling constants in saccharides containing aldofuranosyl (five-membered) rings. In the biologically important β-D-ribofuranosyl and 2-deoxy-β-D-ribofuranosyl (2-deoxy-β-D-*erythro*-pentofuranosyl) rings that were used as models, many of the $^2J_{CCH}$ values associated with coupling pathways involving an endocyclic C−C bond depend linearly on P/π, a measure of ring conformation. In most cases, the endocyclic C−C bond is present in the coupling pathway. In other cases, the $^2J_{CCH}$ value depends linearly on either an adjacent C−C bond torsion angle or shows no systematic relationship with any endocyclic C−C bond torsion angle. In the latter case, secondary (remote) structural effects, defined as those that primarily affect C−C or C−H bond lengths in the C−C−H coupling pathway, cause the $^2J_{CCH}$ value to behave with less predictability. These effects apparently cancel and lead to linearity involving an adjacent C−C bond in some cases. These findings provide a new conceptual framework to understand and exploit the dependencies of geminal $^{13}C-^1H$ NMR spin-couplings on furanose ring conformation. They also reveal the effect of exocyclic C−O bond torsion angles on the magnitudes and signs of $^2J_{CCH}$ values in saccharides, a complication that remains to be addressed before $^2J_{CCH}$ values can be used quantitatively in single- and multi-state *MA'AT* modeling of redundant NMR J-values in furanosyl rings.
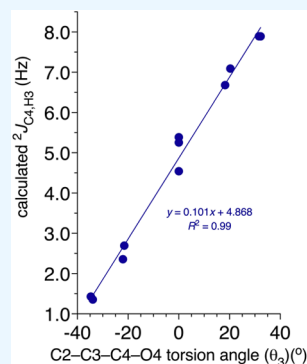
INTRODUCTION

The conformational properties of 2-deoxy-β-D-*erythro*-pentofuranosyl (**1**) and β-D-ribofuranosyl (**2**) rings (Scheme 1) of DNA and RNA, respectively, have been the subject of

Scheme 1. (A) Structures of 2-Deoxy-β-D-*erythro*-pentofuranosyl (1) and β-D-Ribofuranosyl (2) Rings Showing the Five Endocyclic Torsion Angles ($\theta_1-\theta_5$), Atom Numbering, and Assignment of the R and S Hydrogens Attached to C2 and C5 of 1 and C5 of 2; (B) Structures of Methyl 2-Deoxy-β-D-*erythro*-pentofuranoside (3) and Methyl β-D-Ribofuranoside (4) Derived from 1 and 2, Respectively, Where R = OCH₃
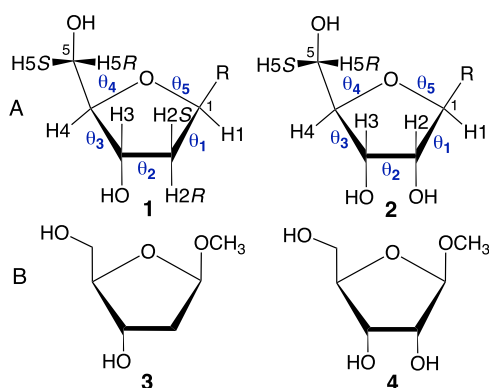
structural studies since the mid-20th century.[1] Seminal work by Altona,[2] Sundaralingam,[3] Harvey,[4] Olson,[5] Wüthrich,[6] Haasnoot,[7] Tinoco[8] and others have laid the foundation for the currently accepted conformational models of these rings, either as free entities or constituents of oligonucleotides and other biomolecules. The results from X-ray crystallography of nucleosides, nucleotides, and oligonucleotides have contributed significantly to the generally accepted two-state conformational models of these rings characterized by exchange between north (N; ^3E; C3′-*endo*) and south (S; ^2E; C2′-*endo*) conformers along a cyclic pseudorotational pathway containing ten envelope (E) and ten twist (T) forms (Scheme 2). This pathway describes N/S exchange via nonplanar conformers, although other studies suggest that this exchange may occur in some cases through the planar conformation (inversion pathway). Validating the X-ray-based N/S model for rings in solution has hinged largely on interpretations of NMR spin-coupling constants (J-couplings). Computational methods such as *PSEUROT*[9] have been commonly used to treat $^3J_{HH}$ values in **1** and **2** in solution but are, by necessity, biased by the

Scheme 2. Pseudorotational Itinerary of a D-Aldofuranose Ring
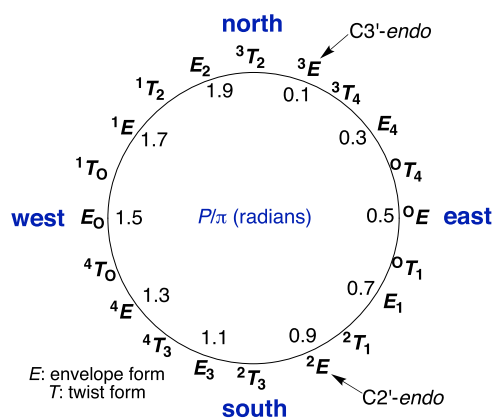
two-state N/S models derived from statistical analyses of crystal structures. This bias stems from the insufficient number of experimental observables from which an independent solution model is derived, that is, a model not biased by the crystallographic findings. While N/S models might apply to **1** and **2** in solution, this model may not describe the solution behaviors of furanosyl rings having different structures,[10,11] since X-ray studies of these rings are limited in number, precluding statistical analyses.
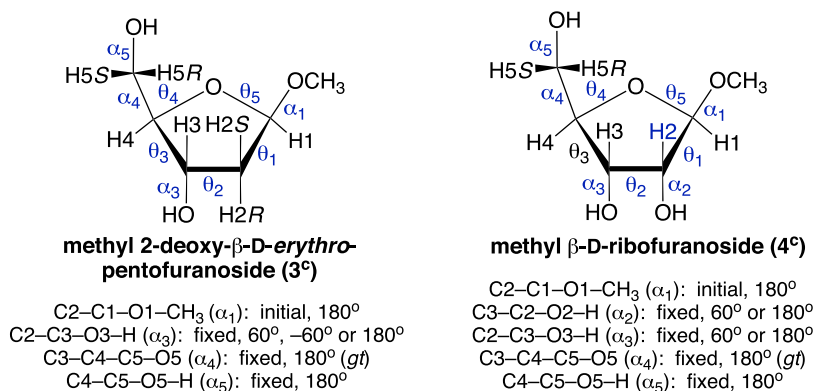
Early work in this laboratory suggested that multiple, redundant J-couplings in furanosyl rings may provide a way to model conformational behavior in solution in an unbiased manner.[12] While methyl 2-deoxy-β-D-*erythro*-pentofuranoside (**3**) and methyl β-D-ribofuranoside (**4**) (Scheme 1) contain three and five $^3J_{HH}$ values sensitive to ring conformation (Tables S1 and S2, Supporting Information), many more J_{CH} and J_{CC} values (30 in **3**, and 23 in **4**) are available, provided that they can be treated quantitatively and, importantly, related to specific endocyclic torsion angles in these rings. Vicinal (three-bond) $^3J_{CH}$ and $^3J_{CC}$ values in **3** and **4** depend primarily on specific θ values (Scheme 1 and Tables S1 and S2, Supporting Information),[13,14] behavior that underpins the recent application of *MA'AT* analysis,[15,16] which provides solution conformational models of these rings in an unbiased fashion.[17] *MA'AT* models can be superimposed on those determined by molecular dynamics (MD) simulation to

validate the latter, which is heretofore difficult or impossible to achieve. Despite these advances, a large number of ^1J and ^2J values in these rings remain unavailable for use in *MA'AT* analysis for several reasons, one being the inability to relate them to one or more endocyclic torsion angles. Unlike vicinal ^3J couplings that obey Karplus or Karplus-like dependencies,[18] one-bond and two-bond (geminal) J-values cannot be easily related to these angles. In this report, we describe new efforts to correlate $^2J_{CCH}$ values in **3** and **4** with specific endocyclic torsion angles $\theta_1 - \theta_5$ (Scheme 1). We show that, for some $^2J_{CCH}$ values, linear relationships exist between the $^2J_{CCH}$ value and one endocyclic torsion angle in the ring and provide structural rationales to explain these relationships. The results advance our understanding of the behavior of $^2J_{CCH}$ values in aldofuranosyl rings in general and potentially provide a new approach to incorporate them in future *MA'AT* modeling. The use of $^2J_{CH}$ values in conjunction with $^3J_{HH}$, $^3J_{CH}$, and $^3J_{CC}$ values will promote more reliable multistate modeling by *MA'AT* analysis.

■ COMPUTATIONAL

Geometric Optimization of Model Glycosides 3^c and 4^c. Density functional theory (DFT) calculations were conducted on model glycosides **3^c** and **4^c** (the superscript "c" denotes *in silico* structures) within *Gaussian*09[19] using the B3LYP functional[20,21] and the 6-31G* basis set[22] for geometry optimization. The effects of solvent water were treated using the self-consistent reaction field (SCRF)[23] and the integral equation formalism (polarizable continuum) model (IEFPCM).[24] As described in detail previously,[17] twenty-one initial structures of **3^c** and **4^c** were built using *GaussView* that corresponded to the ten envelope (*E*), ten twist (*T*), and planar conformers (Scheme 2). For geometry optimization, two of the five endocyclic torsion angles $\theta_1 - \theta_5$ (Scheme 3) were fixed to ensure that the *in silico* structure retained its initial ring conformation. Exocyclic C−C and C−O torsion angles were constrained as shown in Scheme 3. In both structures, the C2−C1−O1−CH$_3$ torsion angle (α_1) was set initially at 180° and allowed to optimize; in all cases, this torsion angle adopted a value of 180 ± 10° in the optimized structures. All of the other torsion angles were fixed during geometry optimization. For **3^c**, three sets of calculations were performed, distinguished by C2−C3−O3−H torsion angles

Scheme 3. Structures of 3^c and 4^c, Definitions of Exo- and Endocyclic Torsion Angles, and Exocyclic Torsion Angle Constraints Used in DFT Calculations[a]

methyl 2-deoxy-β-D-*erythro*-pentofuranoside (3^c)

C2–C1–O1–CH$_3$ (α_1): initial, 180°
C2–C3–O3–H (α_3): fixed, 60°, −60° or 180°
C3–C4–C5–O5 (α_4): fixed, 180° (*gt*)
C4–C5–O5–H (α_5): fixed, 180°

methyl β-D-ribofuranoside (4^c)

C2–C1–O1–CH$_3$ (α_1): initial, 180°
C3–C2–O2–H (α_2): fixed, 60° or 180°
C2–C3–O3–H (α_3): fixed, 60° or 180°
C3–C4–C5–O5 (α_4): fixed, 180° (*gt*)
C4–C5–O5–H (α_5): fixed, 180°

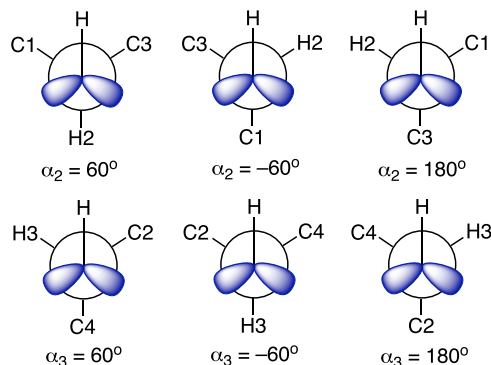[a]For **4^c**, only the 60°/60° and 180°/180° combinations of α_2/α_3 were investigated.

(α_3) fixed at either 60, −60, or 180° in the optimized structures (Scheme 4). For 4^c, only two combinations of C3−

Scheme 4. C2−C3−O3−H (α_3) Rotamers Investigated in DFT Calculations of Methyl 2-Deoxy-β-D-*erythro*-pentofuranoside (3^c)
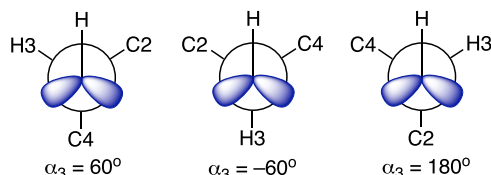
C2−O2−H (α_2) and C2−C3−O3−H (α_3) torsion angles were evaluated: 60°/60° and 180°/180° (Scheme 5). For 3^c, the three sets of calculations gave 63 geometry-optimized conformers, and for 4^c the two sets of calculations gave 42 geometry-optimized conformers.

Scheme 5. C3−C2−O2−H (α_2) and C2−C3−O3−H (α_3) Rotamers in DFT Models of Methyl β-D-Ribofuranoside (4^c)[a]

[a]Only the 60°/60° and 180°/180° combinations of θ_2/θ_3 were studied (see text).

RESULTS AND DISCUSSION

Calculated Dependencies of $^2J_{CCH}$ Values in 3^c and 4^c on the Pseudorotation Phase Angle and Exocyclic C−O Bond Conformation. Furanosyl ring **3** contains eight $^2J_{CCH}$ values that include endocyclic C−C bonds in their C−C−H coupling pathways ($^2J_{C1,H2R}$, $^2J_{C1,H2S}$, $^2J_{C2,H1}$, $^2J_{C2,H3}$, $^2J_{C3,H2R}$, $^2J_{C3,H2S}$, $^2J_{C3,H4}$, and $^2J_{C4,H3}$; Table S1, Supporting Information),
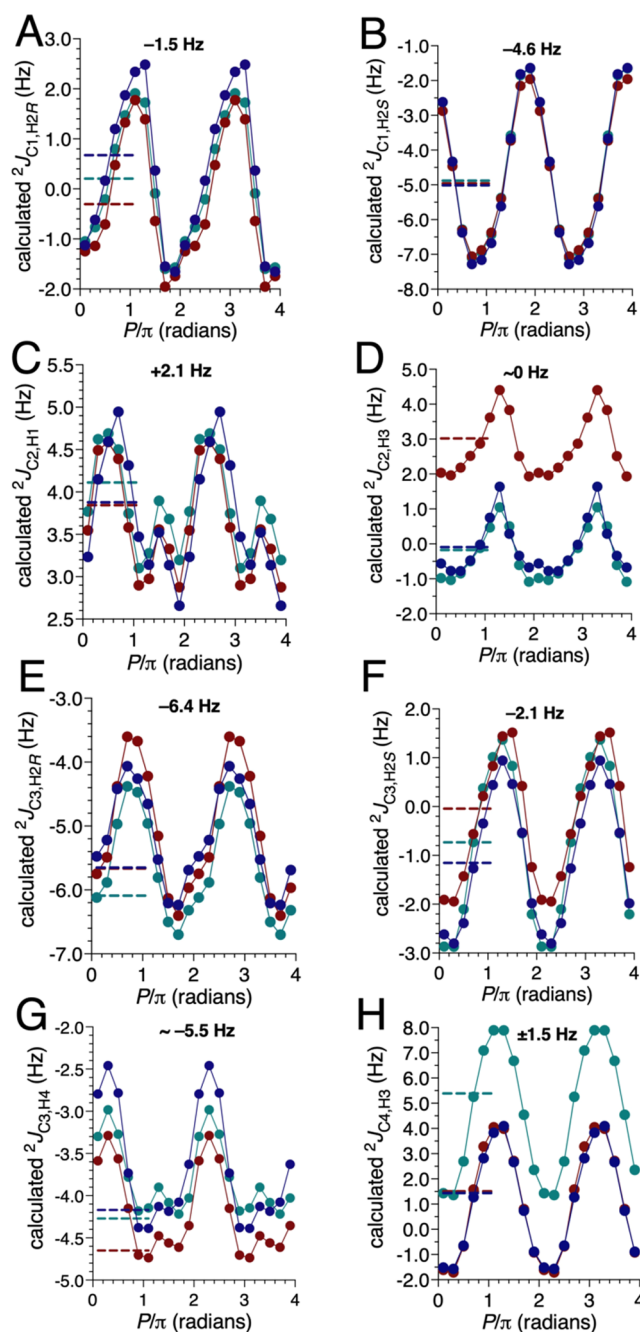
DFT Calculations of NMR Spin-Coupling Constants in 3^c and 4^c. J_{HH}, J_{CH}, and J_{CC} values were calculated in each geometry-optimized structure of 3^c and 4^c using DFT and the B3LYP functional[20,21] in *Gaussian*09.[19] The Fermi contact,[25−27] diamagnetic and paramagnetic spin−orbit, and spin-dipole terms[25] were recovered using a specially designed basis set, [5s2p1d|3s1p],[28,29] and raw (unscaled) calculated couplings are reported and are accurate to within ±0.2−0.3 Hz based on prior work.[30] The self-consistent reaction field (SCRF)[23] and the integral equation formalism (polarizable continuum) model (IEFPCM)[24] were used to treat the effects of solvent water during the *J*-coupling calculations. Plots of the calculated *J*-couplings vs pseudorotation phase angle (*P*) or endocyclic bond angles $\theta_1-\theta_5$ (Scheme 1) were generated using the graphics software, *Prism*.[31]

Figure 1. Plots of calculated $^2J_{CCH}$ values in 3^c as a function of P/π for two cycles of the pseudorotational itinerary (Scheme 2). (A) $^2J_{C1,H2R}$. (B) $^2J_{C1,H2S}$. (C) $^2J_{C2,H1}$. (D) $^2J_{C2,H3}$. (E) $^2J_{C3,H2R}$. (F) $^2J_{C3,H2S}$. (G) $^2J_{C3,H4}$. (H) $^2J_{C4,H3}$. Red points: $\alpha_3 = 60°$. Blue points: $\alpha_3 = −60°$. Green points: $\alpha_3 = 180°$. Curves were generated from spline fits of the data. Dotted lines denote $^2J_{CCH}$ in the planar form. The experimental $^2J_{CCH}$ is shown at the top of each plot (data taken from ref 14).

and furanosyl ring **4** contains six values ($^2J_{C1,H2}$, $^2J_{C2,H1}$, $^2J_{C2,H3}$, $^2J_{C3,H2}$, $^2J_{C3,H4}$, and $^2J_{C4,H3}$; Table S2, Supporting Information). Plots of these values as a function of pseudorotation phase angle, *P*, and exocyclic C−O bond torsion angles, α_2 and/or α_3, are shown in Figures 1 and 2. Four of the eight $^2J_{CCH}$ values in 3^c depend strongly on P/π, exhibiting dynamic ranges of >4 Hz: $^2J_{C1,H2R}$, $^2J_{C1,H2S}$, $^2J_{C3,H2S}$, and $^2J_{C4,H3}$. The strongest dependence is observed for $^2J_{C4,H3}$ (∼6 Hz). $^2J_{C3,H4}$ is negative regardless of the ring conformation, whereas the remaining
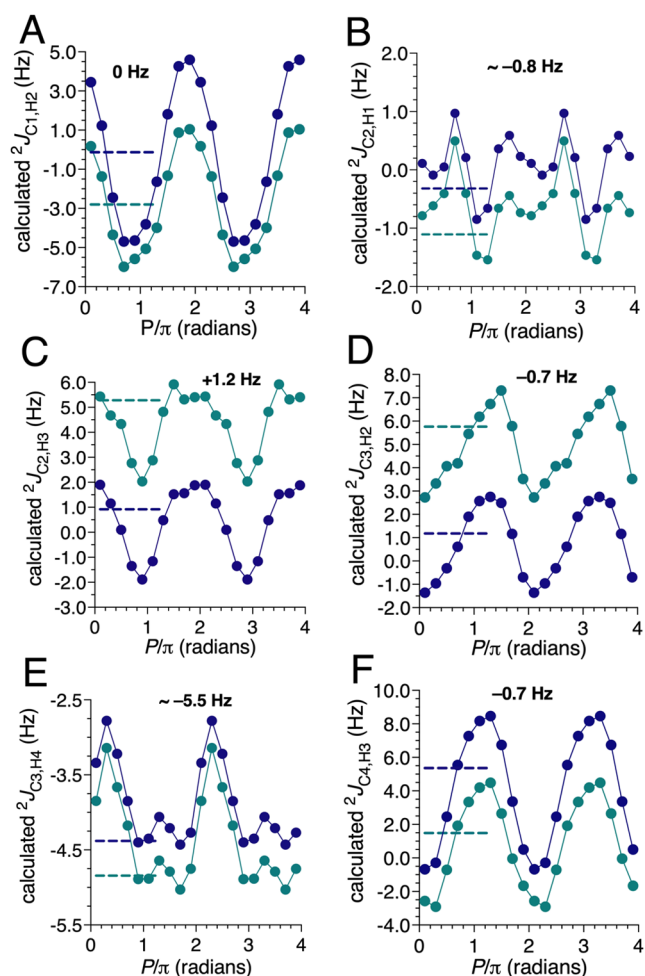
Figure 2. Plots of calculated $^2J_{CCH}$ values in 4^c as a function of P/π for two cycles of the pseudorotational itinerary (Scheme 2). (A) $^2J_{C1,H2}$. (B) $^2J_{C2,H1}$. (C) $^2J_{C2,H3}$. (D) $^2J_{C3,H2}$. (E) $^2J_{C3,H4}$. (F) $^2J_{C4,H3}$. Green points: $\alpha_2/\alpha_3 = 60°/60°$. Blue points: $\alpha_2/\alpha_3 = 180°/180°$. Curves were generated from spline fits of the data. Horizontal dashed lines denote $^2J_{CCH}$ values in the planar form. The experimental $^2J_{CCH}$ is shown at the top of each plot (data taken from ref 14).

Scheme 6. Vicinal Diol Fragment in a Saccharide Highlighting a Geminal C−C−H Coupling Pathway (blue)^a
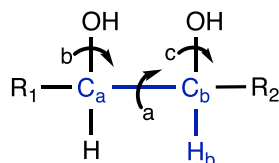
^{a}Rotations about a−c affect $^2J_{Ca,Hb}$. Rotation a exerts a strong configurational or conformational effect. The effect of rotation b can be comparable to that of a. Rotation c least affects $^2J_{Ca,Hb}$. Longer-range structural effects on $^2J_{Ca,Hb}$ may exist and are context-dependent.

seven $^2J_{CCH}$ values are positive or negative depending on the ring conformation.

$^2J_{CCH}$ values involving C3 as a coupled atom ($^2J_{C3,H2R}$, $^2J_{C3,H2S}$, and $^2J_{C3,H4}$) are not much affected by α_3 (change of ~1 Hz). On the other hand, $^2J_{CCH}$ values involving H3 as a coupled atom ($^2J_{C2,H3}$ and $^2J_{C4,H3}$) are significantly affected by α_3, exhibiting y-axis shifts of ~3 Hz. This behavior is consistent with prior work that showed $^2J_{CCH}$ values in saccharides to be

more affected by exocyclic C−O bond rotation when the C−O bond involves the carbon bearing the coupled hydrogen than when the C−O bond involves the coupled carbon (Scheme 6).[32−34] $^2J_{C2,H3}$ shifts to more positive values when $\alpha_3 = 60°$, and $^2J_{C4,H3}$ shifts to more positive values when $\alpha_3 = 180°$. In both cases, the C3−O3 rotamer that orients each of the coupled atoms *anti* to a lone-pair orbital on O3 is associated with more positive (less negative) couplings (Scheme 4). Since lone-pair orbitals *anti* to C−C and C−H bonds are expected to lengthen these bonds (shown below), $^2J_{CCH}$ values appear to become more positive when both bonds are elongated. The shapes of the three curves for $^2J_{C2,H3}$ and $^2J_{C4,H3}$ are conserved, that is, rotation about the C3−O3 bond does not affect the overall dependence of the coupling on P/π; rotating the C3−O3 bond results in a phase shift along the y-axes (the shifted curves can be generated from the remaining two curves by adding a constant to each point on the latter). The relative y-shifts of the curves in Figure 1 caused by changes in α_3 are largely maintained in the planar forms.

Recent *MA'AT* analyses of **3** gave the following two-state conformational model: $58 \pm 3\%\ E_2$ ($P = 345 \pm 5°$) and $42 \pm 3\%\ E_3$ ($P = 198 \pm 5°$).[17] This equilibrium qualitatively explains the experimental $^2J_{CCH}$ values shown in Figure 1. In most cases, the experimental value falls within the range of values predicted by DFT, with two exceptions. The latter include $^2J_{C2,H1}$ and $^2J_{C3,H4}$, where the coupled atoms are proximal to the C1−O1 and C4−C5 bonds in 3^c, respectively, both of which were fixed in one rotameric state in the DFT calculations (Scheme 3). However, in solution, α_1 and α_4 are likely to sample multiple angles, and the measured $^2J_{CCH}$ values will reflect this sampling. Thus, the calculated and experimental values of $^2J_{C2,H1}$ and $^2J_{C3,H4}$ are likely to differ.

Like 3^c, several $^2J_{CCH}$ values show a strong dependence on P/π in 4^c: $^2J_{C1,H2}$, $^2J_{C2,H3}$, $^2J_{C3,H2}$, and $^2J_{C4,H3}$ (Figure 2). These $^2J_{CCH}$ values are also significantly affected by α_2 and α_3. $^2J_{C1,H2}$ shifts to more positive values when α_2 is 180° compared to 60°; the former rotamer orients both C1 and H2 *anti* to a lone-pair orbital on O2. $^2J_{C4,H3}$ shifts to more positive values when α_3 is 180° compared to 60°; the former rotamer orients both C4 and H3 *anti* to an O3 lone-pair orbital. Interpreting the behavior of $^2J_{C2,H3}$ and $^2J_{C3,H2}$ is complicated due to the combined effects of α_2 and α_3. $^2J_{C2,H3}$ is more positive by 3.5−4 Hz in the 60°/60° conformer than in the 180°/180° conformer. In the 60°/60° conformer, two lone-pair orbitals (one each on O2 and O3) are *anti* to the C2−C3 bond, and one O3 lone-pair orbital is *anti* to the C3−H3 bond. In 180°/180°, only one lone-pair orbital is *anti* to the C3−H3 bond. The elongated C2−C3 bond in 60°/60° relative to 180°/180° renders $^2J_{C2,H3}$ more positive. $^2J_{C3,H2}$ is more positive by ~4 Hz in the 60°/60° conformer than in the 180°/180° conformer. In the 60°/60° conformer, two lone-pairs (one each on O2 and O3) *anti* to the C2−C3 bond apparently have a stronger influence than the single O3 lone-pair *anti* to the C2−H2 bond in the 180°/180° conformer.

Recent *MA'AT* analyses of **4** gave the following two-state conformational model: $77 \pm 1\%\ E_2$ ($P = 355 \pm 2°$) and $23 \pm 1\%\ E_3$ ($P = 179 \pm 5°$).[17] As observed for 3^c, most of the experimental $^2J_{CCH}$ values lie within the range of the calculated values, except for $^2J_{C3,H4}$, the latter deviation being attributed to inadequate accounting of the effects of C4−C5 bond rotation (see the discussion above for 3^c). Unlike 3^c, the simple modeling of the conformation about the C1−O1 bond in 4^c is
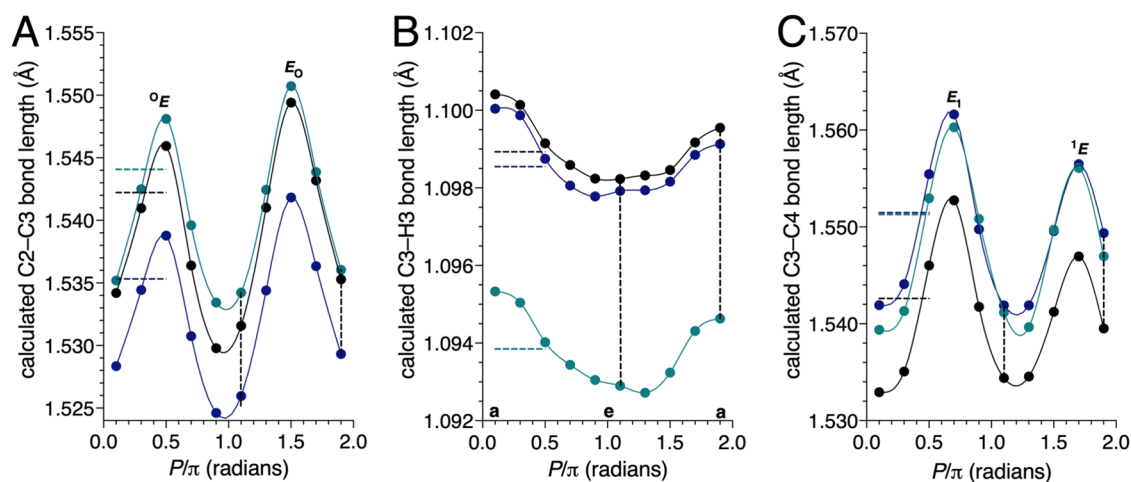
Figure 3. Calculated C2−C3 (A), C3−H3 (B), and C3−C4 (C) bond lengths in **3ᶜ** as a function of P/π. Black: $\alpha_3 = 60°$. Green: $\alpha_3 = -60°$. Blue: $\alpha_3 = 180°$. Curves were generated from spline fits of the data. Horizontal dashed lines denote $^2J_{CCH}$ values in the planar form. Vertical dashed lines identify bond lengths in the E_2 and E_3 conformers (1.9 and 1.1 P/π, respectively).
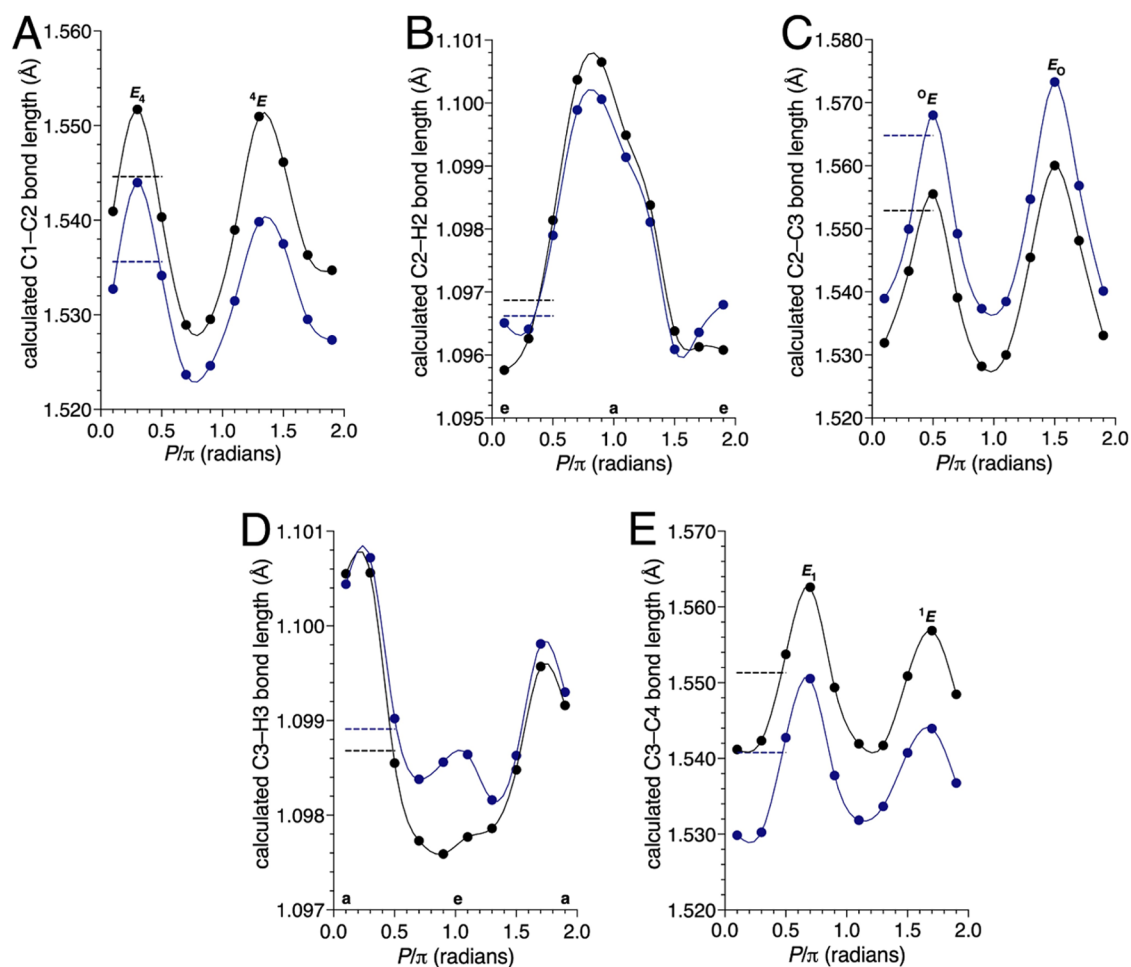

Figure 4. Plots of calculated C−H and C−C bond lengths in **4ᶜ** as a function of P/π. (A) C1−C2 bond. (B) C2−H2 bond. (C) C2−C3 bond. (D) C3−H3 bond. (E) C3−C4 bond. Blue: $\alpha_2/\alpha_3 = 60°/60°$. Black: $\alpha_2/\alpha_3 = 180°/180°$. Curves were generated from spline fits of the data. Horizontal dashed lines denote bond lengths in the planar form.

apparently sufficient to obtain calculated $^2J_{C2,H1}$ values that include the experimental value. While six $^2J_{CCH}$ values in **4ᶜ** are affected by α_2 and α_3 to varying extents, the overall curve shape for any given $^2J_{CCH}$ value is conserved, that is, the pairs of curves in each panel of Figure 2 can be generated by a relatively uniform shift along the y-axis, although the magnitude of the shift depends on the $^2J_{CCH}$ value.

Effects of Ring and Exocyclic C−O Bond Conformations on Bond Lengths in 3ᶜ and 4ᶜ. DFT-calculated C−H and C−C bond lengths in **3ᶜ** and **4ᶜ** depend on P/π (ring
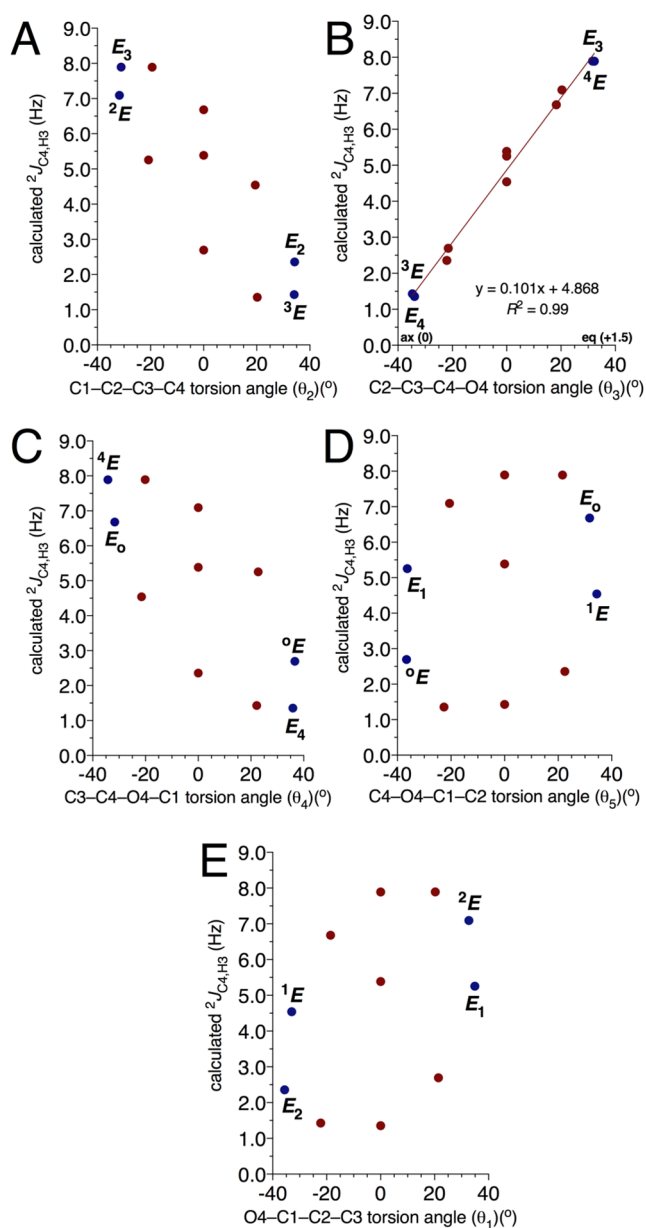
Figure 5. Plots of calculated $^2J_{C4,H3}$ values in 3^c as a function of θ_2 (A), θ_3 (B), θ_4 (C), θ_5 (D), and θ_1 (E). The data in (B) best fit a linear equation, shown with its associated R^2 value. Shown in (B) are the ring conformations, orientations of the C–H bond in the coupling pathway, and PR values associated with $^2J_{CCH}$ values at the extrema of the plot. The $\alpha_3 = 180°$ data set was used to generate these plots (see the text for details).

conformation) and on α_2 and/or α_3 (Figures 3 and 4). As observed for J-couplings in Figure 1, the overall curve shape is essentially unaffected by α_3 in 3^c (the three curves shift on the y-axis by roughly a fixed amount) (Figure 3). The C2–C3 bond length decreases significantly when $\alpha_3 = 180°$ relative to 60° and −60°, that is, in the rotamer lacking an O3 lone-pair orbital *anti* to the C2–C3 bond (Scheme 4). The C3–H3 bond length decreases sharply when $\alpha_3 = -60°$ relative to 60 and 180°, that is, in the rotamer lacking an O3 lone-pair orbital *anti* to the C3–H3 bond (Scheme 4). Finally, the C3–C4 bond length decreases appreciably when $\alpha_3 = 60°$ relative to −60 and 180°, that is, in the rotamer lacking an O3 lone-pair orbital *anti* to the C3–C4 bond (Scheme 4). The C2–C3 and

C3–C4 bond lengths reach maxima in ring conformers in which the out-of-plane atom lies "across" from the C–C bond (i.e., O4 for C2–C3 and C1 for C3–C4). The C3–H3 bond length is affected by bond orientation, with *quasi*-equatorial bonds in S forms shorter than the *quasi*-axial bonds in N forms.[35]

The C3–O3 rotamer (α_3) in 3^c that orients each of the coupled atoms *anti* to an O3 lone-pair orbital is associated with the more positive (less negative) $^2J_{C2,H3}$ and $^2J_{C4,H3}$ values (Scheme 4). It was argued above that the more positive couplings are associated with longer C–C and C–H bonds in the C–C–H coupling pathway. DFT calculations confirm this correlation. For example, for $\alpha_3 = 60°$, C2 and H3 are both *anti* to an O3 lone-pair orbital and both the C2–C3 and C3–H3 bonds are elongated. Likewise, for $\alpha_3 = 180°$, C4 and H3 are both *anti* to the O3 lone-pair orbital, and both the C3–H3 and C3–C4 bonds are elongated.

In 4^c, $^2J_{C1,H2}$ is more positive when α_2 is 180° rather than when it is 60°; as expected, the C1–C2 bond is longer when α_2 = 180° instead of when it is 60° (Figure 4A). $^2J_{C4,H3}$ is more positive when α_3 is 180° rather than when it is 60°; the C3–C4 bond is longer when α_3 = 180° as opposed to when it is 60° (Figure 4E). For $^2J_{C2,H3}$, $r_{C2,C3}$ is larger in the 60°/60° rotamer than in the 180°/180° rotamer, and appears to explain the more positive coupling in the former (Figure 4C). For $^2J_{C3,H2}$, more positive coupling is observed in the 60°/60° rotamer containing two lone-pair orbitals (one each on O2 and O3) *anti* to the C2–C3 bond, as opposed to the 180°/180° rotamer containing a single O3 lone-pair *anti* to the C2–H2 bond. The results in Figure 4B,C shows a larger $r_{C2,C3}$ in the 60°/60° rotamer, while both the 60°/60° and 180°/180° rotamers show similar behavior for $r_{C2,H2}$. At first glance, the results in Figure 4B appear problematic in that $r_{C2,H2}$ should be larger in the 180°/180° rotamer than in 60°/60° rotamer because of the *anti* O2 lone-pair orbital found in the former but not in the latter (a vicinal lone-pair effect[35]). In the 60°/60° rotamer, $r_{C2,H2}$ should be shorter due to the lack of a vicinal lone-pair effect and no significant 1,3 lone-pair effects[32] from O3. On the other hand, in the 180°/180° rotamer, the vicinal lone-pair effect, which lengthens the C2–H2 bond, is probably offset by 1,3 lone-pair effects from one of the lone-pair orbitals on O3, which shorten the bond. Presumably, this synergism causes the C2–H2 bond length to behave similarly in 60°/60° and 180°/180° rotamers. This result points to complications that arise in predicting C–H bond lengths in saccharides, since competing lone-pair effects cause both bond elongation and bond contraction. In furanose rings, the relative contributions of the longer-range 1,3 and 1,4 lone-pair effects[36] will depend on ring conformation.

Application of the Projection Rule to $^2J_{CCH}$ Values in 3 and 4. The projection rule[37] has proven useful in predicting the magnitudes and signs of $^2J_{CCH}$ values in aldopyranosyl rings.[38,39] This rule was applied to **3** and **4** to predict the behavior of $^2J_{CCH}$ values in representative north (E_2) and south (E_3) ring conformations (Tables S3 and S4, Supporting Information). For **3**, projection (PR) values range from −1 (e.g., $^2J_{C1,H2S}$ in E_3) to +1.5 (e.g., $^2J_{C4,H3}$ in E_3). Qualitatively, $^2J_{CCH}$ values predicted by the projection rule are in general agreement with the corresponding DFT-calculated values. For example, $^2J_{C3,H2R}$ is predicted to be −5 Hz in E_2 and E_3, and DFT gives averaged values of −6.0 and −4.6 Hz, respectively. Likewise, $^2J_{C2,H1}$ is predicted to be ∼2 Hz in E_2 and E_3, and DFT gives averaged values of 2.9 and 3.2 Hz, respectively. In
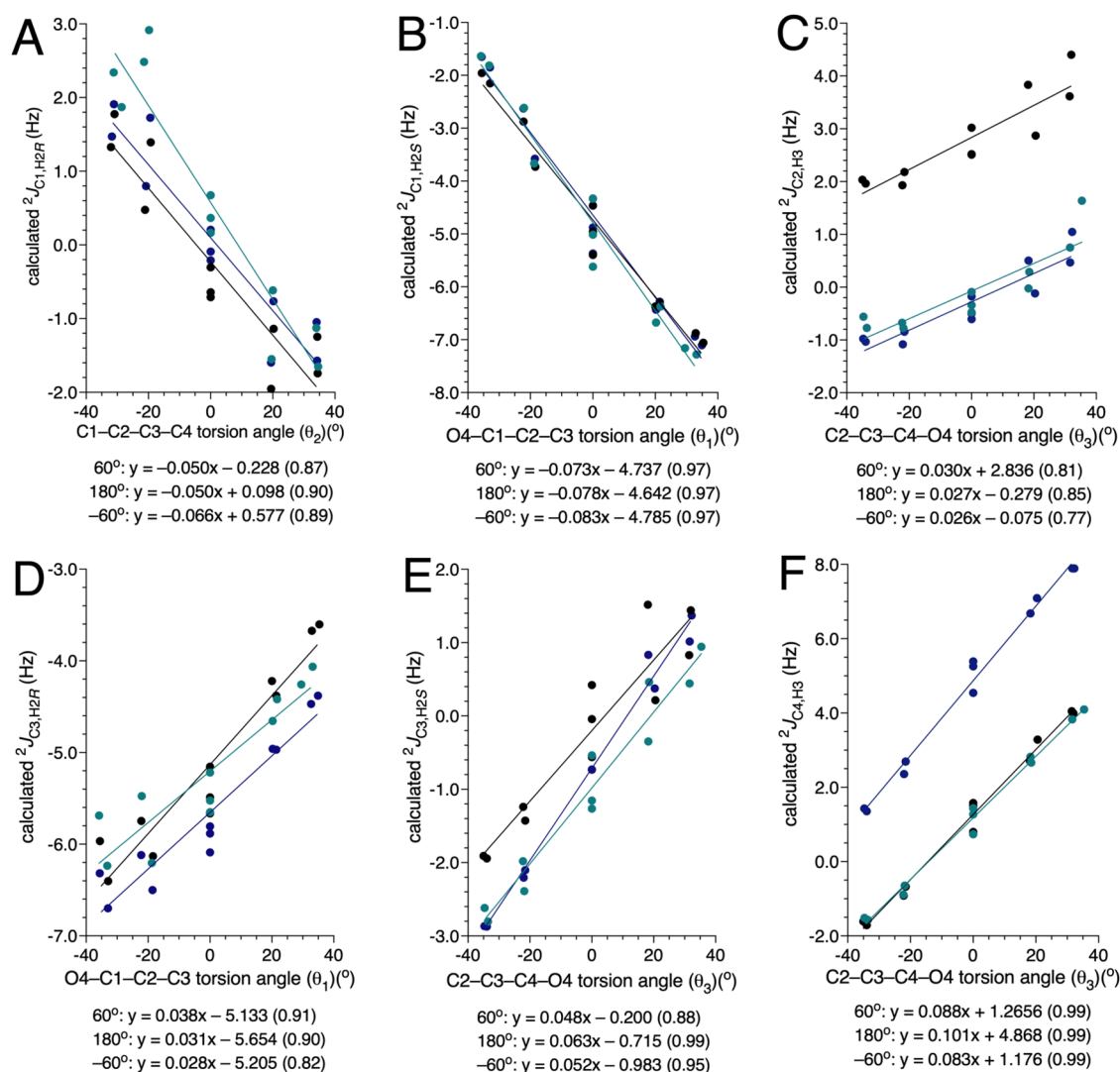
Figure 6. Plots of calculated $^2J_{CCH}$ values in $\mathbf{3^c}$ as a function of $\theta_1-\theta_3$. (A) $^2J_{C1,H2R}$ vs θ_2. (B) $^2J_{C1,H2S}$ vs θ_1. (C) $^2J_{C2,H3}$ vs θ_3. (D) $^2J_{C3,H2R}$ vs θ_1. (E) $^2J_{C3,H2S}$ vs θ_3. (F) $^2J_{C4,H3}$ vs θ_3. Black: $\alpha_3 = 60°$. Blue: $\alpha_3 = 180°$. Green: $\alpha_3 = -60°$. The three data sets in each graph were fit by linear least-squares and gave the equations and R^2 values (in parentheses) shown below each plot.

all cases, PR-calculated $^2J_{CCH}$ values are within ∼2 Hz of the corresponding value calculated by DFT. Coupling trends determined by the projection rule are consistent with those determined by DFT. For example, $^2J_{C1,H2S}$ is predicted by the projection rule to be ∼0 Hz in E_2 and −8 Hz in E_3, while DFT calculations yield average values of −1.7 and −6.5 Hz, respectively; both methods indicate that the coupling is considerably more negative in the south (E_3) conformer.

Application of the projection rule to $^2J_{CCH}$ values in **4** gave results similar to those obtained for **3**. Qualitatively, differences in the magnitudes and signs of specific $^2J_{CCH}$ values in E_2 and E_3 predicted by the projection rule are maintained in the DFT-calculated $^2J_{CCH}$ (Table S4, Supporting Information). For example, the projection rule predicts that $^2J_{C1,H2}$ will change from 2 to −5 Hz as the ring changes from E_2 to E_3. DFT calculations yield a change from 2.8 to −4.5 Hz.

While the projection method provides useful information about *J*-coupling trends, PR-calculated $^2J_{CCH}$ values are not accurate, as revealed by the range of DFT-calculated $^2J_{CCH}$ values associated with projections of 0. According to the projection rule, these $^2J_{CCH}$ values should be ∼−2 Hz, but

DFT calculations give values that range from +1.4 to −4.7 Hz (Tables S3 and S4, Supporting Information).

Correlation between Ring Endocyclic Torsion Angles and $^2J_{CCH}$ Values in $\mathbf{3^c}$ and $\mathbf{4^c}$. The plots shown in Figures 1 and 2 provide information on the effects of ring conformation on $^2J_{CCH}$ values in $\mathbf{3^c}$ and $\mathbf{4^c}$, and while these plots can be parametrized,[34] we investigated potential structural correlations that might exist between $^2J_{CCH}$ values and the ring endocyclic torsion angles $\theta_1-\theta_5$ (Scheme 1) defined as follows: $\theta_1 =$ O4−C1−C2−C3, $\theta_2 =$ C1−C2−C3−C4, $\theta_3 =$ C2−C3−C4−O4, $\theta_4 =$ C3−C4−O4−C1, and $\theta_5 =$ C4−O4−C1−C2 (Schemes 1 and 3). Each endocyclic $^2J_{CCH}$ value in $\mathbf{3^c}$ and $\mathbf{4^c}$ was plotted against these five angles in the 20 nonplanar and the planar forms. An example is shown in Figure 5 for $^2J_{C4,H3}$ in $\mathbf{3^c}$. Four of the five plots contained significant scatter and a characteristic "circular" behavior (Figure 5A,C−E). One plot (Figure 5B) that correlates $^2J_{C4,H3}$ with θ_3 produced a nearly linear relationship, giving a least-squares fit with a correlation coefficient of 0.99. Similar treatments of the remaining seven $^2J_{CCH}$ values in $\mathbf{3^c}$ ($\alpha_3 = 180°$) and the six $^2J_{CCH}$ values in $\mathbf{4^c}$

Scheme 7. Six Intra-ring $^2J_{CCH}$ Values in 3[c] That Show a Linear Dependence on One of the Ring Endocyclic Torsion Angles (Shown in Blue)[a]
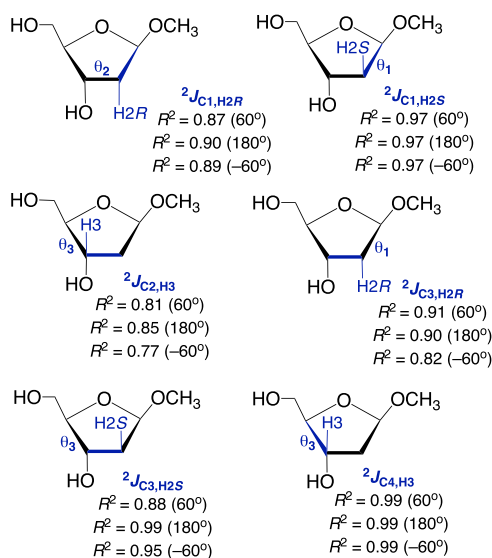
[a]The C−C−H coupling pathways are highlighted in blue. R^2 values were obtained from data on α_3 rotamers (Scheme 4) in Figure 6

($\alpha_2/\alpha_3 = 60°/60°$) are shown in Figures S1−S13 (Supporting Information).

Of the eight calculated $^2J_{CCH}$ values in 3[c], six show linear dependencies on one of the endocyclic torsion angles $\theta_1-\theta_5$ (Figure 6 and Scheme 7) regardless of the value of α_3. Correlation coefficients obtained from linear least-squares fits ranged from 0.77 to 0.99. $^2J_{C1,H2S}$, $^2J_{C3,H2S}$, and $^2J_{C4,H3}$ show particularly strong linear relationships to θ_1, θ_3, and θ_3, respectively, giving correlation coefficients of 0.9 or greater (Figure 6 and Scheme 7). The slopes of the fit lines are relatively independent of α_3, although there are exceptions.

Of the six $^2J_{CCH}$ values in 4[c], four show a linear dependence on one of the endocyclic torsion angles $\theta_1-\theta_5$ (Figure 7 and Scheme 8). The plots in Figure 7 include the $\alpha_2/\alpha_3 = 60°/60°$ and $180°/180°$ data sets for comparison. Correlation coefficients ranged from 0.76 to 0.96. $^2J_{C1,H2}$ and $^2J_{C4,H3}$ exhibit particularly strong linear relationships to θ_1 and θ_3, respectively, giving correlation coefficients of 0.9 or greater. In general, the slopes of the fit lines are relatively independent of α_2/α_3, especially for $^2J_{C2,H3}$ and $^2J_{C3,H2}$.

Structural Explanation of Linear Relationships between $^2J_{CCH}$ and θ Values in 3[c] and 4[c]. The plots in Figures 6 and 7 show that the magnitudes of some $^2J_{CCH}$ values in 3[c] and 4[c] scale linearly with specific endocyclic torsion angles θ. An inspection of Figure 5A−E shows that, for $^2J_{C4,H3}$ in 3, the plots become increasingly linear in the order $\theta_5 \approx \theta_1 \rightarrow \theta_4 \approx \theta_2 \rightarrow \theta_3$, with the θ_3 plot (Figure 5B) giving the best fit. $^2J_{C4,H3}$ in 4 behaves similarly, scaling almost linearly when plotted against θ_3 (Figure 7D). In both cases, the central bond comprising the θ_3 torsion angle is the C3−C4 bond within the C4−C3−H3 coupling pathway. However, this behavior is not observed uniformly in compounds 3 and 4. For example, $^2J_{C3,H2S}$ in 3, and the structurally related $^2J_{C3,H2}$ in 4, show strong linear correlations with θ_3, not θ_2 (Schemes 7 and 8).

In 3 (and 4), the $^3E/E_4$ conformers (N forms) are associated with the most negative values of θ_3, while the $E_3/^4E$ conformers (S forms) are associated with the most positive

values (Figure 8). In 3 and 4, $^2J_{C4,H3}$ becomes more positive as θ_3 changes from ∼−40 to ∼40°. The remaining envelope and planar forms of 3 (and 4) distribute symmetrically along the plot, as shown in Figure 8, that is, $^2J_{C4,H3}$ becomes more positive in the following order: $^3E/E_4 < {}^0E/E_2 < P/E_1/^1E < {}^2E/E_0 < E_3/^4E$. Newman projections of the C3−C4 bonds in 3 and 4 in $^3E/E_4$ and $E_3/^4E$ conformations are shown in Scheme 9. The PR value associated with $^3E/E_4$ is ∼0 and that associated with $E_3/^4E$ is ∼1.5. These values correlate with $^2J_{CCH}$ values of ∼−2 and +4 Hz, respectively. The $^0E/E_2$ pair gives identical Newman projections and PR values of ∼+0.5. The $P/E_1/^1E$ group gives identical Newman projections and PR values of ∼1.0. The $^2E/E_0$ pair gives identical Newman projections with a PR value of ∼1.3.

To test whether the empirical observations made in Figure 8 are observed generally, a similar plot of $^2J_{C1,H2}$ in 4 was examined (Figure 9) since this $^2J_{CCH}$ depends linearly on θ_1, which, like $^2J_{C4,H3}$ in 3, contains a central C−C bond that resides in the C1−C2−H2 coupling pathway. As found for $^2J_{C4,H3}$ in 3, PR values differ significantly at the plot extrema, with the $E_2/^1E$ and $^2E/E_1$ conformers giving values of ∼1.0 and ∼−0.5, respectively, for an overall change (1.5) identical to that found for $^2J_{C4,H3}$ in 3 (Figure 8). The $^3E/E_0$ pair, the $P/E_4/^4E$ group, and the $^0E/E_3$ pair yield PR values of ∼0.5, ∼0, and ∼−0.3, respectively. There is a systematic change in PR values from $\theta_1 = -40$ to 40°. The poorer fit of the data to a linear equation compared to that in Figure 8 is caused by the $P/E_4/^4E$ group, where identical PR values are associated with calculated $^2J_{C1,H2}$ values that span ∼3 Hz. This behavior suggests that the relative orientations of C5 and O3 with respect to the C1−C2−H2 coupling pathway exert different secondary effects on $^2J_{C1,H2}$. This observation is key to understanding the $^2J_{CCH}$ behavior, as discussed below. Nevertheless, the behavior of $^2J_{C1,H2}$ in 4 closely mimics that of $^2J_{C4,H3}$ in 3.

Having shown that some $^2J_{CCH}$ values in 3 and 4 depend linearly on ring endocyclic torsion angles when the central bond of the angle coincides with the C−C bond in the coupling pathway, a case where this relationship is not observed was examined, namely, $^2J_{C3,H2S}$ in 3 (Figures 6E and 10). As shown in Figures 8 and 9, the distribution of conformers along the line is symmetric, with $P/^1E/E_1$ forms at the center, $E_0/^2E$ and $^0E/E_2$ pairs bracketing them, and the extrema occupied by the $^4E/E_3$ and $^3E/E_4$ pairs. However, the plot differs in that, within any pair or group, PR values differ by as much as 1 unit, although average PR values increase systematically from ∼−0.25 to ∼0.9 as θ_3 changes from −40 to 40°. This behavior reveals the limitations of the projection method to predict $^2J_{CCH}$ values in structures like 3 and 4. The method assumes that the local structure primarily determines these J-values, since only oxygens attached to the two carbons in the coupling pathway are considered when calculating PR values. The results in Figure 10 point to contributions from longer-range interactions. For example, $^2J_{C3,H2S}$ values in ^0E and E_2 are associated with PR values of ∼0.5 and ∼−0.5, respectively, that correlate with predicted J-values of ∼0 and ∼−5 Hz, respectively. However, the corresponding DFT-calculated values are nearly identical at ∼−2 Hz. Linear plots where the endocyclic torsion angle does not contain the C−C bond in the coupling pathway appear to be associated with $^2J_{CCH}$ values that are subject to significant secondary structural effects. Secondary effects on some $^2J_{CCH}$ values are small such that considering only local oxygens (i.e., those appended to the
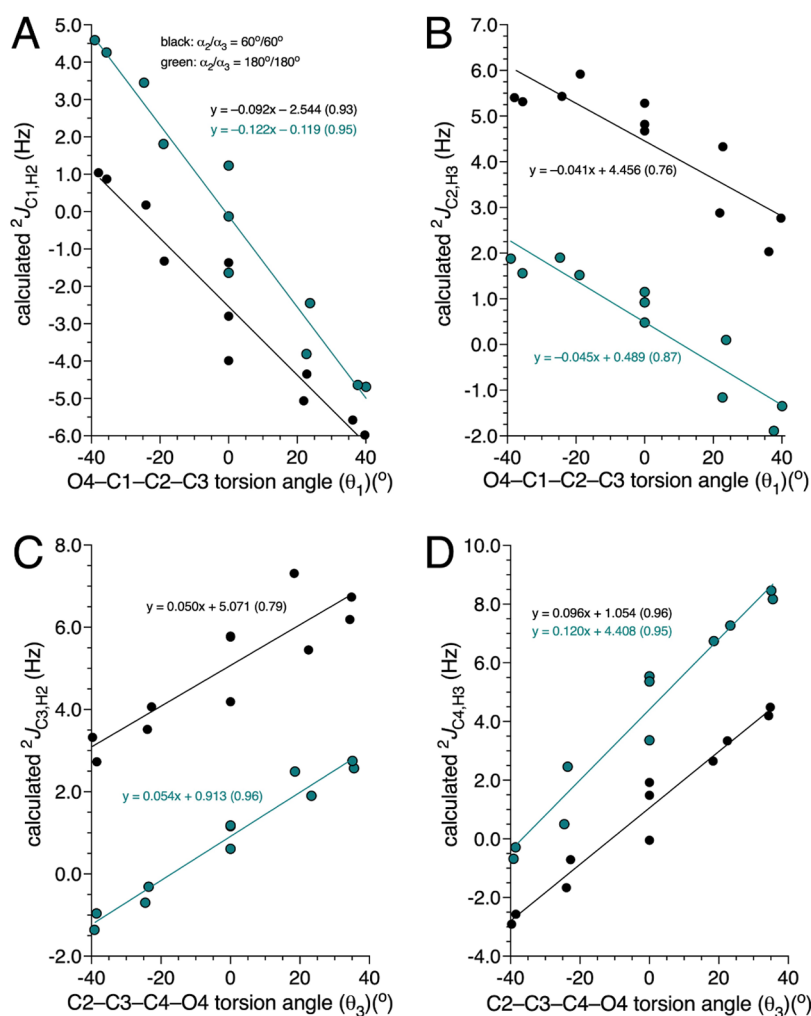
Figure 7. Plots of calculated $^2J_{CCH}$ values in 4^c as a function of ring endocyclic torsion angles θ_1 or θ_3. (A) $^2J_{C1,H2}$ vs θ_1. (B) $^2J_{C2,H3}$ vs θ_1. (C) $^2J_{C3,H2}$ vs θ_3. (D) $^2J_{C4,H3}$ vs θ_3. Black: $\alpha_2/\alpha_3 = 60°/60°$. Green: $\alpha_2/\alpha_3 = 180°/180°$. The two data sets in each plot were fit by linear least-squares, giving equations and R^2 values (in parentheses) shown in each plot.

Scheme 8. Four Intra-ring $^2J_{CCH}$ Values in 4^c That Exhibit an Approximately Linear Dependence on One of the Ring Endocyclic Torsion Angles (Shown in Blue)[a]
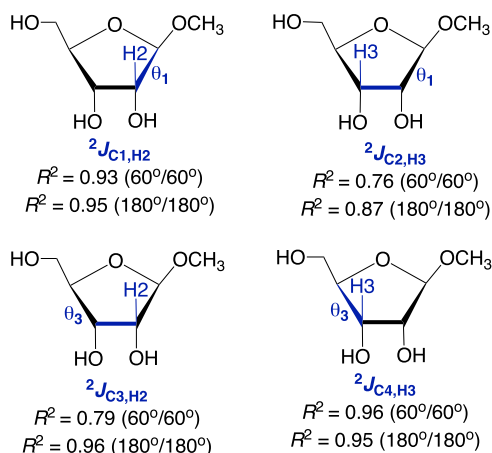
[a]The C−C−H coupling pathways are highlighted in blue. R^2 values were obtained from data on α_2/α_3 rotamers (Scheme 5) shown in Figure 7
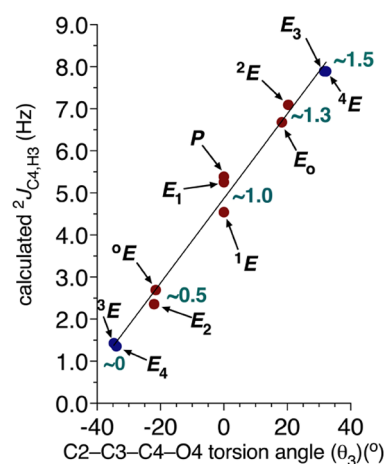

Figure 8. Plot in Figure 5B showing calculated $^2J_{C4,H3}$ values in 3^c associated with the ten envelope (E) and planar (P) conformers, and PR values (in green) associated with the five clusters of points distributed along the line. Data pertain to the $\alpha_3 = 180°$ rotamer of 3 (see Scheme 4).

two carbons) is sufficient to give relatively reliable $^2J_{CCH}$ values predicted by the PR method. For other $^2J_{CCH}$ values, secondary

Scheme 9. Newman Projections for the C3−C4 Bond in 3 and 4 in the $^3E/E_4$ and $E_3/^4E$ Conformers, Showing PR Values Used to Predict $^2J_{C4,H3}$ Values in Both Conformers
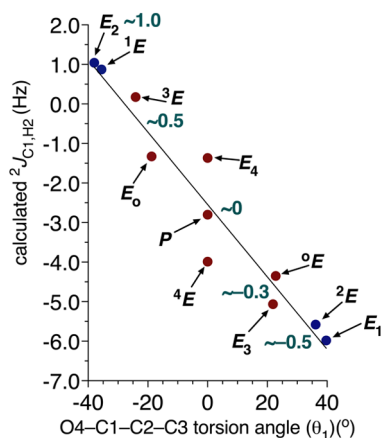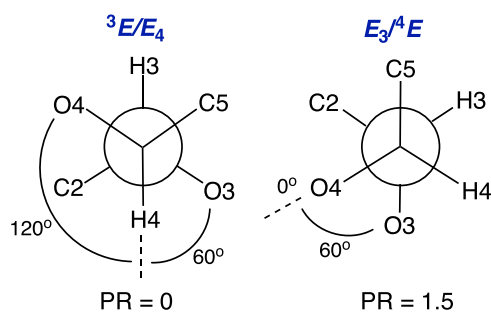

Figure 9. Plot in Figure 7A showing calculated $^2J_{C1,H2}$ values in $\mathbf{4^c}$ associated with the ten envelope (E) and planar (P) conformers, and PR values (in green) associated with the five clusters of points distributed along the line. Data pertain to the $\alpha_2/\alpha_3 = 60°/60°$ rotamer of $\mathbf{4^c}$ (see Scheme 5).
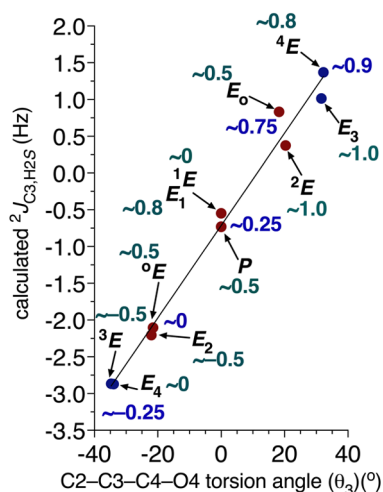

Figure 10. Plot shown in Figure 6E showing calculated $^2J_{C3,H2S}$ values in $\mathbf{3^c}$ associated with the ten envelope (E) and planar (P) conformers and PR values (in green) associated with the five clusters of points distributed along the line. The numbers shown in blue are averaged PR values for each cluster. Data pertain to the $\alpha_3 = 180°$ rotamer of $\mathbf{3^c}$ (see Scheme 4).

effects are large enough to produce better linear dependencies on endocyclic torsion angles containing a central C−C bond adjacent to that in the coupling pathway. This shift to an

adjacent C−C bond presumably reduces or cancels these secondary effects. On the other hand, for some $^2J_{CCH}$ values, this shift is ineffective, leading to greater data scatter and poorer linear fits.

■ CONCLUSIONS

Vicinal (three-bond) NMR scalar coupling constants have enjoyed widespread use to determine the conformations of molecules in solution. This usage is based on the well-known relationship between their magnitudes and the dihedral angles subtended by the coupled nuclei (Karplus relationships[18]). In saccharides, $^3J_{HH}$ ($^3J_{HCCH}$, $^3J_{HCOH}$, and $^3J_{HCNH}$) and $^3J_{CH}$ ($^3J_{COCH}$, $^3J_{CCCH}$, $^3J_{CCOH}$, and $^3J_{CCNH}$) values have been used to investigate various conformational features of molecules (e.g., conformations of O-glycosidic linkages,[30] pyranosyl and furanosyl rings,[17] and exocyclic N-acetyl[40] and hydroxymethyl[41] groups). In contrast, geminal (two-bond) J-couplings are less well understood and less used as conformational constraints, with the exception of $^2J_{HCH}$.[29] In this report, we described new relationships between $^2J_{CCH}$ values and ring conformation in two biologically relevant aldopentofuranosyl rings, leading to an improved understanding of how these J-couplings might be applied in future investigations of these and related rings. The work was motivated by the desire to maximize the number of NMR J-couplings used in MA'AT analyses of these rings[17] to permit the testing of both single- and multistate conformational models in solution determined exclusively from treatments of redundant NMR J-couplings using circular statistics.[16,17]

We found that, in many but not all cases, $^2J_{CCH}$ values in which the C−C bond in the C−C−H coupling pathway contributes to the furanosyl ring structure are related linearly to the rotational state of the C−C bond. This finding suggests that concerted use of these relationships could lead to conformational models of the ring in solution, especially when used in conjunction with MA'AT analysis. The findings reinforce the known relationships between pyranosyl ring configuration and $^2J_{CCH}$ coupling magnitude and sign,[37,42,43] encoded in the projection rule developed by Pedersen and co-workers.[37] In the present case, rotation about an endocyclic C−C bond in furanosyl rings is limited yet systematic as the ring undergoes pseudorotation, leading in many cases to linear relationships between $^2J_{CCH}$ values and a specific endocyclic C−C bond torsion angle.

While linear relationships between $^2J_{CCH}$ values and endocyclic torsion angles involving the C−C bond in the coupling pathway are often observed, they are not uniformly observed. In some cases, linear relationships are observed involving an endocyclic C−C bond adjacent to that found in the coupling pathway. In other cases, a linear relationship is not observed for any endocyclic C−C bond in the ring. These differences in behavior are attributed to the influence of secondary (remote) structural effects on $^2J_{CCH}$ values that vary in strength and can significantly affect the $^2J_{CCH}$ magnitude. These effects, discussed elsewhere,[32,36] probably result from changes in C−C and C−H bond lengths in the coupling pathway, in some cases leading to better linearity, presumably through fortuitous random cancelation, when an adjacent endocyclic C−C bond torsion is correlated with the $^2J_{CCH}$ value.

As shown previously,[28,32] $^2J_{CCH}$ values involving carbons bearing hydroxyl groups (vicinal diol fragments) are affected by the conformational properties of the two C−O bonds, with

rotation about the C−O bond involving the carbon bearing the coupled hydrogen exerting greater effects than the rotation of the C−O bond involving the coupled carbon (Scheme 6). In the context of the present work, this behavior is illustrated in Figure 1D,H for two $^2J_{CCH}$ values in $\mathbf{3}^c$ (those involving H3 as the coupled hydrogen). The displacement of the curves relating these $^2J_{CCH}$ values to P/π is caused by lone-pair effects of O3 on the C−C and C−H bond lengths in the coupling pathway. While overall curve shape is conserved (i.e., independent of the rotational state of the C3−O3 bond), the effect of exocyclic C3−O3 bond rotation on the absolute values of the $^2J_{CCH}$ cannot be ignored. Similar effects are found in $\mathbf{4}$ (Figure 2C,D). Consequently, quantitative interpretations of experimental $^2J_{CCH}$ values will depend on prior knowledge of the rotameric populations of exocyclic C−O bonds in some cases. This knowledge remains rudimentary from an experimental perspective at present. It is hoped that *MA'AT* analysis will shed light on this problem through the application of redundant *J*-couplings sensitive to the conformational properties of exocyclic C−O bonds. This knowledge would promote the use of $^2J_{CCH}$ values in experiment-based conformational modeling of saccharides and related molecules in solution.

◼ ASSOCIATED CONTENT

Ⓢ Supporting Information

The Supporting Information is available free of charge at https://pubs.acs.org/doi/10.1021/acsomega.4c11358.

> Plots of $^2J_{C1,H2R}$ against $\theta_1−\theta_5$ in $\mathbf{3}^c$; plots of $^2J_{C1,H2S}$ against $\theta_1−\theta_5$ in $\mathbf{3}^c$; plots of $^2J_{C2,H1}$ against $\theta_1−\theta_5$ in $\mathbf{3}^c$; plots of $^2J_{C2,H3}$ against $\theta_1−\theta_5$ in $\mathbf{3}^c$; plots of $^2J_{C3,H2R}$ against $\theta_1−\theta_5$ in $\mathbf{3}^c$; plots of $^2J_{C3,H2S}$ against $\theta_1−\theta_5$ in $\mathbf{3}^c$; plots of $^2J_{C3,H4}$ against $\theta_1−\theta_5$ in $\mathbf{3}^c$; plots of $^2J_{C1,H2}$ against $\theta_1−\theta_5$ in $\mathbf{4}^c$; plots of $^2J_{C2,H1}$ against $\theta_1−\theta_5$ in $\mathbf{4}^c$; plots of $^2J_{C2,H3}$ against $\theta_1−\theta_5$ in $\mathbf{4}^c$; plots of $^2J_{C3,H2}$ against $\theta_1−\theta_5$ in $\mathbf{4}^c$; plots of $^2J_{C3,H4}$ against $\theta_1−\theta_5$ in $\mathbf{4}^c$; plots of $^2J_{C4,H3}$ against $\theta_1−\theta_5$ in $\mathbf{4}^c$; NMR spin-couplings sensitive to $\theta_1−\theta_5$ in $\mathbf{3}$; NMR spin-couplings sensitive to $\theta_1−\theta_5$ in $\mathbf{4}$; properties of $^2J_{CCH}$ values in the E_2 and E_3 conformers of $\mathbf{3}$; properties of $^2J_{CCH}$ values in the E_2 and E_3 conformers of $\mathbf{4}$; and representative Cartesian coordinates for $\mathbf{3}^c$ and $\mathbf{4}^c$ (PDF)

◼ AUTHOR INFORMATION

Corresponding Author

Anthony S. Serianni − *Department of Chemistry and Biochemistry, University of Notre Dame, Notre Dame, Indiana 46556-5670, United States;* ⓞ orcid.org/0000-0001-6114-1446; Email: aseriann@nd.edu

Authors

Reagan J. Meredith − *Texas Biomedical Research Institute, San Antonio, Texas 78227-0549, United States; Department of Chemistry and Biochemistry, University of Notre Dame, Notre Dame, Indiana 46556-5670, United States;* ⓞ orcid.org/0000-0001-7330-3190

Ian Carmichael − *Department of Chemistry and Biochemistry, University of Notre Dame, Notre Dame, Indiana 46556-5670, United States; Radiation Laboratory, University of Notre Dame, Notre Dame, Indiana 46556-5670, United States*

Complete contact information is available at:

https://pubs.acs.org/10.1021/acsomega.4c11358

◼ REFERENCES

(1) Saenger, W. *Principles of Nucleic Acid Structure*; Springer-Verlag: New York, 1984.

(2) Haasnoot, C. A. G.; De Leeuw, F. A. A. M.; De Leeuw, H. P. M.; Altona, C. The Relationship Between Proton-Proton NMR Coupling Constants and Substituent Electronegativities. II. Conformational Analysis of the Sugar Ring in Nucleosides and Nucleotides in Solution Using a Generalized Karplus Equation. *Org. Magn. Reson.* **1981**, *15*, 43−52.

(3) Altona, C.; Sundaralingam, M. Conformational Analysis of the Sugar Ring in Nucleosides and Nucleotides. New Description Using the Concept of Pseudorotation. *J. Am. Chem. Soc.* **1972**, *94*, 8205−8212.

(4) Harvey, S. C.; Prabhakaran, M. Ribose Puckering: Structure, Dynamics, Energetics and the Pseudorotation Cycle. *J. Am. Chem. Soc.* **1986**, *108*, 6128−6136.

(5) Olson, W. K. How Flexible is the Furanose Ring? 2. An Updated Potential Energy Estimate. *J. Am. Chem. Soc.* **1982**, *104*, 278−286.

(6) Szyperski, T.; Fernandez, C.; Ono, A.; Kainosho, M.; Wüthrich, K. Measurement of Deoxyribose $^3J_{HH}$ Scalar Couplings Reveals Protein Binding-Induced Changes in the Sugar Puckers of the DNA. *J. Am. Chem. Soc.* **1998**, *120*, 821−822.

(7) Raap, J.; van Boom, J. H.; van Lieshout, H. C.; Haasnoot, C. A. G. Conformations of Methyl 2-Deoxy-β-D-ribofuranoside and Methyl β-D-Ribofuranoside: A Proton Magnetic Resonance Spectroscopy and Molecular Mechanics Study. *J. Am. Chem. Soc.* **1988**, *110*, 2736−2743.

(8) Hines, J. V.; Landry, S. M.; Varani, G.; Tinoco, I., Jr. Carbon-Proton Scalar Couplings in RNA: 3D Heteronuclear and 2D Isotope-Edited NMR of a ^{13}C-Labeled Extra-Stable Hairpin. *J. Am. Chem. Soc.* **1994**, *116*, 5823−5831.

(9) De Leeuw, F. A. A. M.; Altona, C. Computer-Assisted Pseudorotation Analysis of Five-Membered Rings by Means of Proton Spin−Spin Coupling Constants: Program PSEUROT. *J. Comput. Chem.* **1983**, *4*, 428−437.

(10) Westhof, E.; Sundaralingam, M. A Method for the Analysis of Puckering Disorder in Five-Membered Rings: The Relative Mobilities of Furanose and Proline Rings and Their Effects on Polynucleotide and Polypeptide Backbone Flexibility. *J. Am. Chem. Soc.* **1983**, *105*, 970−976.

(11) Olson, W. K. Three-State Models of Furanose Pseudorotation. *Nucleic Acids Res.* **1981**, *9*, 1251−1262.

(12) Serianni, A. S.; Barker, R. [^{13}C]-Enriched Tetroses and Tetrofuranosides: An Evaluation of the Relationship Between NMR Parameters and Furanosyl Ring Conformation. *J. Org. Chem.* **1984**, *49*, 3292−3300.

(13) Podlasek, C. A.; Stripe, W. A.; Carmichael, I.; Shang, M.; Basu, B.; Serianni, A. S. ^{13}C-^{1}H Spin-Coupling Constants in the β-D-Ribofuranosyl Ring: Effect of Ring Conformation on Coupling Magnitudes. *J. Am. Chem. Soc.* **1996**, *118*, 1413−1425.

(14) Church, T. J.; Carmichael, I.; Serianni, A. S. ^{13}C-^{1}H and ^{13}C-^{13}C Spin-Coupling Constants in Methyl β-D-Ribofuranoside and Methyl 2-Deoxy-β-D-*erythro*-pentofuranoside: Correlations with Mo-

lecular Structure and Conformation. *J. Am. Chem. Soc.* **1997**, *119*, 8946−8964.

(15) Meredith, R. J.; Sernau, L.; Serianni, A. S. *MA'AT*: A Web-Based Application to Calculate Rotamer Population Distributions from Nuclear Magnetic Resonance Spin-Coupling Constants. *J. Chem. Inf. Model.* **2022**, *62*, 3135−3141.

(16) Meredith, R. J.; Carmichael, I.; Woods, R. J.; Serianni, A. S. *MA'AT* Analysis: Probability Distributions of Molecular Torsion Angles in Solution from NMR Spectroscopy. *Acc. Chem. Res.* **2023**, *56*, 2313−2328.

(17) Meredith, R. J.; McGurn, M.; Euell, C.; Rutkowski, P.; Cook, E.; Carmichael, I.; Serianni, A. S. *MA'AT* Analysis of Aldofuranosyl Rings: Unbiased Modeling of Conformational Equilibria and Dynamics in Solution. *Biochemistry* **2022**, *61*, 239−251.

(18) Karplus, M. Contact Electron-Spin Coupling of Nuclear Magnetic Moments. *J. Chem. Phys.* **1959**, *30*, 11−15.

(19) Frisch, M. J.; Trucks, G. W.; Schlegel, H. B.; Scuseria, G. E.; Robb, M. A.; Cheeseman, J. R.; Scalmani, G.; Barone, V.; Mennucci, B.; Petersson, G. A.et al. *Gaussian09*; Gaussian, Inc.: Wallingford, CT, 2009.

(20) Becke, A. D. Density-Functional Thermochemistry. III. The Role of Exact Exchange. *J. Chem. Phys.* **1993**, *98*, 5648−5652.

(21) Becke, A. D. New Mixing of Hartree-Fock and Local Density-Functional Theories. *J. Chem. Phys.* **1993**, *98*, 1372−1377.

(22) Hehre, W. J.; Ditchfield, R.; Pople, J. A. Self-Consistent Molecular Orbital Methods. XII. Further Extensions of Gaussian-Type Basis Sets for Use in Molecular Orbital Studies of Organic Molecules. *J. Chem. Phys.* **1972**, *56*, 2257−2261.

(23) Cancès, E.; Mennucci, B.; Tomasi, J. A New Integral Equation Formalism for the Polarizable Continuum Model: Theoretical Background and Applications To Isotropic and Anisotropic Dielectrics. *J. Chem. Phys.* **1997**, *107*, 3032−3041.

(24) Cammi, R.; Mennucci, B.; Tomasi, J. Fast Evaluation of Geometries and Properties of Excited Molecules In Solution: A Tamm-Dancoff Model With Application to 4-Dimethylaminobenzonitrile. *J. Phys. Chem. A* **2000**, *104*, 5631−5637.

(25) Sychrovský, V.; Gräfenstein, J.; Cremer, D. Nuclear Magnetic Resonance Spin−Spin Coupling Constants from Coupled Perturbed Density Functional Theory. *J. Chem. Phys.* **2000**, *113*, 3530−3547.

(26) Helgaker, T.; Watson, M.; Handy, N. C. Analytical Calculation of Nuclear Magnetic Resonance Indirect Spin−Spin Coupling Constants at the Generalized Gradient Approximation and Hybrid Levels of Density-Functional Theory. *J. Chem. Phys.* **2000**, *113*, 9402−9409.

(27) Barone, V.; Peralta, J. E.; Contreras, R. H.; Snyder, J. P. DFT Calculation of NMR J_{FF} Spin Spin Coupling Constants in Fluorinated Pyridines. *J. Phys. Chem. A* **2002**, *106*, 5607−5612.

(28) Klepach, T.; Zhao, H.; Hu, X.; Zhang, W.; Stenutz, R.; Hadad, M. J.; Carmichael, I.; Serianni, A. S. Informing Saccharide Structural NMR Studies With Density Functional Theory Calculations. In *Glycoinformatics: Methods in Molecular Biology*; Lütteke, T.; Frank, M., Eds.; Springer: New York, 2015; pp 289−331.

(29) Stenutz, R.; Carmichael, I.; Widmalm, G.; Serianni, A. S. Hydroxymethyl Group Conformation in Saccharides: Structural Dependencies of $^2J_{HH}$, $^3J_{HH}$ and $^1J_{CH}$ Spin-Spin Coupling Constants. *J. Org. Chem.* **2002**, *67*, 949−958.

(30) Zhang, W.; Turney, T.; Meredith, R.; Pan, Q.; Sernau, L.; Wang, X.; Hu, X.; Woods, R. J.; Carmichael, I.; Serianni, A. S. Conformational Populations of β-(1→4) *O*-Glycosidic Linkages Using Redundant NMR *J*-Couplings and Circular Statistics. *J. Phys. Chem. B* **2017**, *121*, 3042−3058.

(31) *Prism 8 for Mac OS X*, version 8.4.2 829 (464); GraphPad Software, April 18, 2020.

(32) Klepach, T. E.; Carmichael, I.; Serianni, A. S. Geminal $^2J_{CCH}$ Spin-Spin Coupling Constants as Probes of the ϕ Glycosidic Torsion Angle in Oligosaccharides. *J. Am. Chem. Soc.* **2005**, *127*, 9781−9793.

(33) Meredith, R. J.; Carmichael, I.; Serianni, A. S. Nonconventional NMR Spin-Coupling Constants in Oligosaccharide Conformational

Modeling: Structural Dependencies Determined from Density Functional Theory Calculations. *ACS Omega* **2022**, *7*, 23950−23966.

(34) Meredith, R. J.; Zhang, W.; Yoon, M.-K.; Hu, X.; Carmichael, I.; Serianni, A. S. *MA'AT* Analysis of the *O*-Glycosidic Linkages of Oligosaccharides Using Nonconventional NMR *J*-Couplings: *MA'AT* and MD Models of *Phi*. *RSC Adv.* **2024**, *14*, 30286−30294.

(35) Serianni, A. S.; Wu, J.; Carmichael, I. One-Bond ^{13}C-^{1}H Spin-Coupling Constants in Aldofuranosyl Rings: Effect of Conformation on Coupling Magnitude. *J. Am. Chem. Soc.* **1995**, *117*, 8645−8650.

(36) Cloran, F.; Zhu, Y.; Osborn, J.; Carmichael, I.; Serianni, A. S. 2-Deoxy-β-D-ribofuranosylamine: Quantum Mechanical Calculations of Molecular Structure and NMR Spin-Spin Coupling Constants in Nitrogen-Containing Saccharides. *J. Am. Chem. Soc.* **2000**, *122*, 6435−6448.

(37) Bock, K.; Pedersen, C. Two- and Three-Bond ^{13}C-^{1}H Couplings in Some Carbohydrates. *Acta Chem. Scand.* **1977**, *31b*, 354−358.

(38) Podlasek, C. A.; Wu, J.; Stripe, W. A.; Bondo, P. B.; Serianni, A. S. [^{13}C]-Enriched Methyl Aldopyranosides: Structural Interpretations of ^{13}C-^{1}H Spin-Coupling Constants and ^{1}H Chemical Shifts. *J. Am. Chem. Soc.* **1995**, *117*, 8635−8644.

(39) Serianni, A. S.; Podlasek, C. A. ^{13}C-^{1}H Spin-Coupling Constants in Carbohydrates: Magnitude and Sign Determinations via 2D NMR Methods. *Carbohydr. Res.* **1994**, *259*, 277−282.

(40) Meredith, R. J.; Tetrault, T.; Yoon, M.-K.; Zhang, W.; Carmichael, I.; Serianni, A. S. *N*-Acetyl Side-Chain Conformation in Saccharides: Solution Models Obtained from *MA'AT* Analysis. *J. Org. Chem.* **2022**, *87*, 8368−8379.

(41) Meredith, R. J.; Yoon, M.-K.; Carmichael, I.; Serianni, A. S. *MA'AT* Analysis: Unbiased Multi-State Conformational Modeling of Exocyclic Hydroxymethyl Group Conformation in Methyl Aldohexopyranosides. *J. Phys. Chem. B* **2024**, *128*, 2360−2370.

(42) Schwarcz, J. A.; Perlin, A. S. Orientational Dependance of Vicinal and Geminal ^{13}C-^{1}H Coupling. *Can. J. Chem.* **1972**, *50*, 3667−3676.

(43) Schwarcz, J. A.; Cyr, N.; Perlin, A. S. Orientation Effects and the Sign of Two-Bond ^{13}C-^{1}H Coupling. *Can. J. Chem.* **1975**, *53*, 1872−1875.